Z. Angew. Math. Phys. (2018) 69:105

0044-2275/18/040001-16
published online July 27, 2018
https://doi.org/10.1007/s00033-018-1000-3

Zeitschrift für angewandte Mathematik und Physik ZAMP

Material characterization and computations of a polymeric metamaterial with a pantographic substructure

Hua Yang, Gregor Ganzosch, Ivan Giorgio and B. Emek Abali

Abstract. The development of additive manufacturing methods, such as 3D printing, allows the design of more complex architectured materials. Indeed, the main structure can be obtained by means of periodically (or quasi-periodically) arranged substructures which are properly conceived to provide unconventional deformation patterns. These kinds of materials which are 'substructure depending' are called *metamaterials*. Detailed simulations of a metamaterial is challenging but accurately possible by means of the elasticity theory. In this study, we present the steps taken for analyzing and simulating a particular type of metamaterial composed of a pantographic substructure which is periodic in space—it is simply a grid. Nevertheless, it shows an unexpected type of deformation under a uniaxial shear test. This particular behavior is investigated in this work with the aid of direct numerical simulations by using the finite element method. In other words, a detailed mesh is generated to properly describe the substructure. The metamaterial is additively manufactured using a common polymer showing nonlinear elastic deformation. Experiments are undertaken, and several hyperelastic material models are examined by using an inverse analysis. Moreover, a direct numerical simulation is repeated for all studied material models. We show that a good agreement between numerical simulations and experimental data can be attained.

Mathematics Subject Classification. 74A30, 74B20, 74S05.

Keywords. Nonlinear elasticity, Metamaterials, Material identification, Hyperelastic models.

1. Introduction

Additive manufacturing provides an advanced fabrication technique to produce prototypes with geometries showing high degree of complexity [26,48]. Additionally, this technique enables to generate architectures constituted of the so-called microscopic elements. Such a substructure (cellular architecture) modifies the macroscopic deformation behavior completely. The ultimate aim is to carefully design a functional material in a macroscale manifesting novel type of a deformation pattern affected by the substructure charactering the microscale [43,51]. The new conceived material is called metamaterial, and its deformation behavior depends not only on its material characteristic but also upon the substructure. This macroscopic deformation behavior of metamaterials has been studied by several groups, see e.g., [13,20]. A possible modeling has been achieved by using a discrete model based on the microscopic elements in [5,19,73,75]. Another approach is to model the metamaterial directly in the macroscale. In this case, we need to introduce new parameters allowing the material model to take into account the new pattern of deformation. This generalized method is characterized by different features depending on the kinematic descriptors used. Among these models we can cite, for example, micropolar medium [29–31], strain gradient theory [3,22,44,49,52,56,58,60], microstructured continuum [3,7,28,53], couple stress material [50,71], peridynamics [27], for historical remarks see [21] and for a recent review see [70]. It is of paramount importance to emphasize that the theory of elasticity is valid and accurate in the microscale, the introduction of new structure-related parameters are necessary as a homogenization procedure resulting in higher-order terms in the formulation. As easily said, it is not yet clear how these

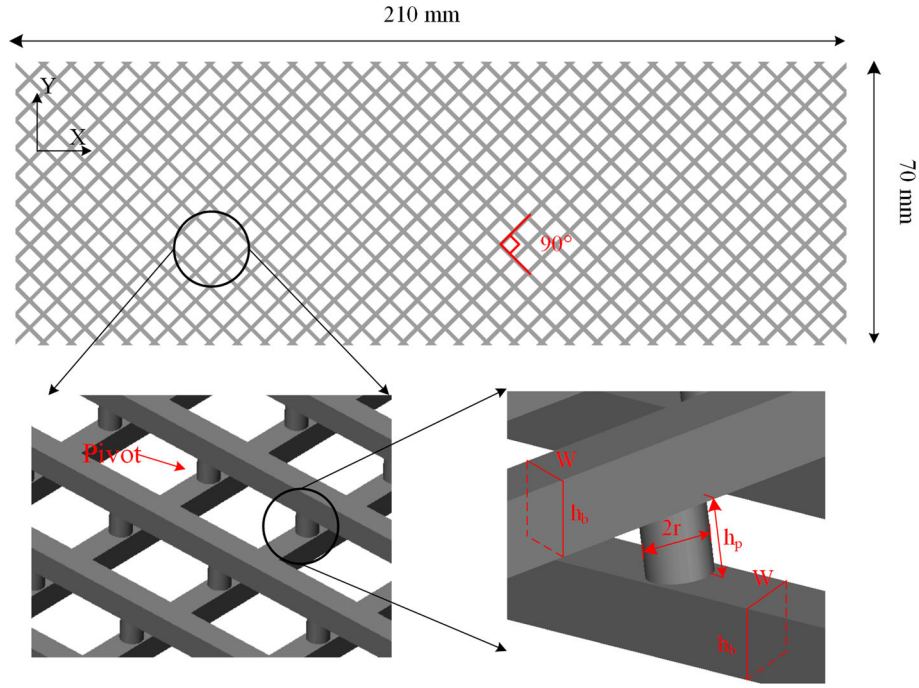

FIG. 1. Geometry of pantographic structures

structure-related parameters can be obtained directly out of the microscopic elements. Simply stated, we fail to know these structure-related parameters. It is worth noting that mesoscale approaches are available, in which the 'micro'-elements are modeled with the help of continuous theories as beams or plates [9].

Consider a so-called pantographic structure as shown in Fig. 1 (see for more details [25,62]). The structure is constituted by two parallel arrays of beams connected by internal cylinders called pivots. Such a design is well known in trusses or scissor structures; interestingly, this substructure can be used to investigate the aforementioned generalized method [17,23,24,57]. The continuum approach to describe such type of metamaterial is based, for the noticeable geometric similarities, on the fabric material theory (see e.g., [14,15,55,66,69]). We emphasize that the structure-related parameters are not known. Recently, a simple shear test on a 3D printed pantographic structure has been investigated in [12]. The uncommon deformation behavior of this structure is the main focus in this work. For a rigorous understanding of the characteristics of the pantographic substructure, we aim at a direct numerical simulation by using the finite element method (FEM). The detailed modeling of the underlying substructure results in a high computational cost [34]. However, we only need an appropriate constitutive equation for the bulk material of the substructure produced by a 3D printer with polyamide (PA). This polymer shows a hyperelastic behavior that is modeled by a stored energy function depending on nonlinear strain measures, among others see [10,11,38,40,67,76].

The metamaterial under a uniaxial shear test has been described in Sect. 2. For the material properties, a sample out of the metamaterial has been examined under a uniaxial tensile test in Sect. 3. Inverse analysis is explained and used to obtain the material parameters. In Sect. 4, FEM implementation is shown and computations are obtained by implementing various hyperelastic models with the aid of open-source codes developed under the FEniCS project, see [37,45]. A comparison of the experiments and computations is presented in Sect. 5.

TABLE 1. *Geometry sizes of the microstructure*

w in mm	h_b in mm	r in mm	h_p in mm
1.00	1.00	0.45	1.00

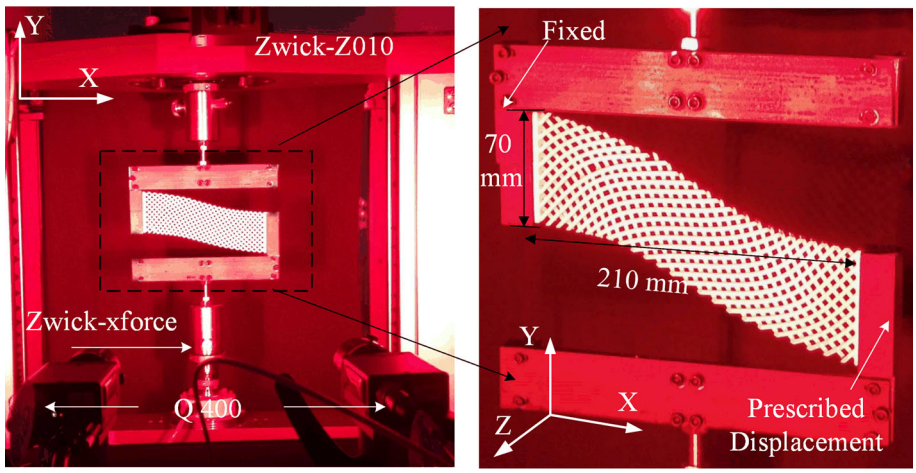

FIG. 2. Setup of the shearing test

2. Uniaxial shear experiments

The pantographic structure has been analyzed in a simple shear test [33]. Displacement-controlled shearing experiments under large deformations were carried out on the 3D printed metamaterial. For generating the structure, CAD model of the structure in STL format has been used as the input file for the 3D printer, Formiga P 100 from EOS GmbH in Munich, Germany. Polyamide powder (PA2200) was employed to produce the samples. Sample possesses macroscopic dimensions of 210 mm×70 mm, while the distance between two adjacent pivots is 0.495 mm. It is further characterized by 4 geometrical parameters as shown in Fig. 1 and quantified in Table 1.

The setup of the shearing experiment is presented in Fig. 2. For the shearing test, Zwick Z010 has been employed that is equipped with a load cell (Zwick-Xforce) capable of recording the reaction force in the range of ± 10 kN with the accuracy of 20 N (equal of 0.2%). One edge of the pantographic structure was fixed to the adaption device, and the other edge was driven in parallel to itself by a loading rate of 15 mm/min up to 70 mm. We remark that the structure is of the same size regarding the maximum displacement on the boundary, and therefore, the structure is under large deformation. The displacement data were acquired by a displacement sensor with an accuracy of ± 2.0 µm. Moreover, an optical measurement device Q-400 has been utilized with 4 cameras in order to record the 3D deformation during the shearing tests. The used cameras capture pictures at a rate of 0.5 Hz with a resolution of 1600×1200 pixels. As post-processing, all pictures are exploited for obtaining a 3D extraction of emerging displacements. Of course, this optical measurement system implements a non-contact (non-invasive) procedure. The pantographic structure clearly showed a nonlinear reaction response during the shearing tests; details will be presented in the upcoming Sect. 4.

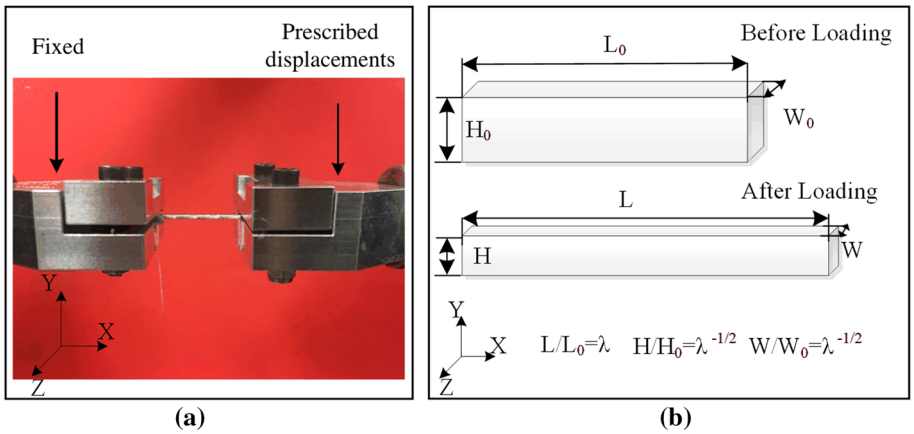

FIG. 3. Uniaxial tensile test setup: picture of the sample (left), drawing of the geometry (right)

3. Modeling and parameter identification of the polymer used in 3D printing

The manufacturing method of the metamaterial is based on laser sintering of the polyamide powder in layer by layer. A laser is used to increase the temperature of the powder at a particular location. Increased temperature yields to a local melting of the material and forming a covalent binding to the neighboring structure. After a subsequent cooling down, the sinter powdered polyamide forms a solid structure. Even in the case of a 'perfect' production without porosity or heterogeneity, the material obtained might show a different response than the powder material, since the cooling rate during the 3D printing modifies the chain density in a polymer. We fail to know the constitutive equation for the laser-sintered PA forming the pantographic structure and aim at investigating as well as determining an appropriate constitutive model depicting the characteristics of the laser-sintered polyamide material (PA2200).

Technically, in order to ensure the accuracy of predictions, a range of standard experiments like uniaxial, equibiaxial tension, pure shear tests, *etc.*, are necessary. As stated in [42], there is an insignificant difference between the predictions based on uniaxial experiments and combination of uniaxial, biaxial, and planar tests. In this section, we perform uniaxial tests, use an inverse analysis for obtaining the material parameters, and choose an appropriate model for further investigations solely based on the uniaxial tensile test results.

3.1. Uniaxial tensile tests for 3D printed PA2200 beams

Three samples were cut from the pantographic structure, and uniaxial tensile tests were undertaken as shown in Fig. 3. One side was clamped and the other side was pulled with the prescribed displacement by using a feedback controller. The loading rate leads to 15 mm/min of a velocity, and the test was ended with a rupture. Reaction force was recorded by a load cell attached to the testing device. The measured quantities are displacement and force. Often the force is divided by the initial surface area to obtain the engineering stress; analogously, the displacement is divided by the initial length for acquiring a strain. A nonlinear relation between strain and stress signalizes the necessity of a hypo- or hyperelastic material model. Average of conducted tests can be depicted in Fig. 4. The stress–strain plot is shown for a possible comparison with the literature. The initial tangent modulus, 500 MPa, is calculated from the slope of the stress–strain curve at small strains up to 0.5%. This modulus can be seen as equivalent to Young's modulus for the linear elastic regime. Obviously, the material response is nonlinear. Moreover,

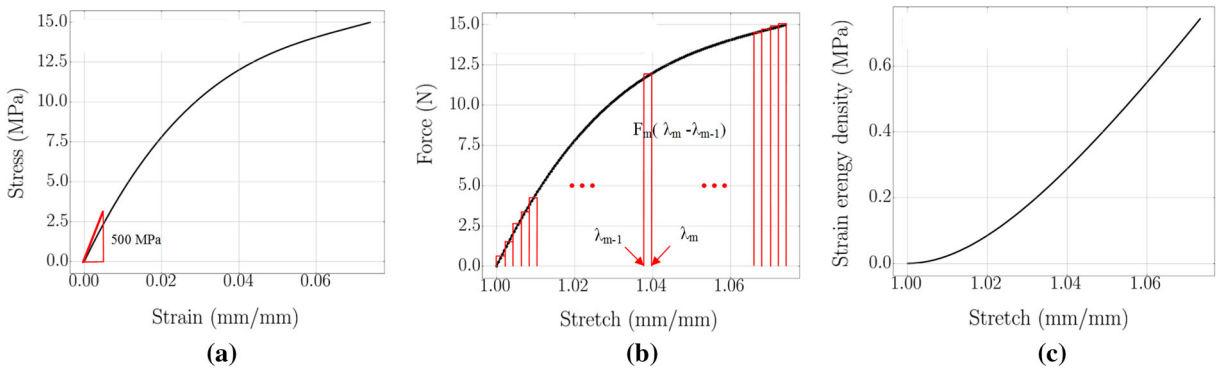

FIG. 4. Uniaxial tensile tests: **a** stress versus strain; **b** force versus stretch; **c** strain energy density versus stretch

from the inspection and comparison of the cross section before and after rupture, we observed that the area reduction is insignificant. By using the micrograph of the beam in Fig. 5, the width changed only 23.3 μm (2.2%). Therefore, it is reasonable to assume that the cross-sectional area reduction is negligible and an elastic behavior up to the final deformation is preserved such that we assume a brittle fracture at the end of the experiment. Consequently, we need a hyperelastic constitutive equation. Owing to large deformations, these stress and strain measures are not accurate, and thus, we avoid using them and employ an inverse analysis based on force, F, and displacement, u. As exhibited in Fig. 4b, c, we compute the stored energy density W by evaluating,

$$W = \frac{1}{V_0}\int F\,\mathrm{d}u = \frac{1}{A_0}\int F\,\mathrm{d}\lambda, \tag{3.1}$$

with the stretch $\lambda = L/L_0$ ($\mathrm{d}\lambda = \mathrm{d}u/L_0$) normalized by the initial length L_0 and cross-sectional area A_0. Herein we assume that the material is isochoric, i.e., the volume remains the same throughout the deformation. For n (possibly equidistant) points, we calculate the integral numerically,

$$W_m = \sum_{m=1}^{n} \frac{F_m(\lambda_m - \lambda_{m-1})}{A_0} \tag{3.2}$$

in which W_m, F_m, and λ_m represent the value of strain energy density, force, and stretch, respectively, at the point m with a total of n points. In Fig. 4c, we display the stored energy evaluated as described foregoing.

We remark that, even if the elastic behavior seems dominant, the influence of viscoelastic, or damage, or plastic phenomena occurring during the experiments are not negligible and their role should be further investigated. In [68,74], some helpful ideas and a first attempt to deal with such issues specifically for a pantographic structure are presented. A more general framework to address this study of quasi-static brittle fracture is presented in [59,61,63]. We refer to [6,8,18,36] for a useful bibliography about the viscoelastic effect.

3.2. Hyperelastic models

We use the standard continuum mechanical notation and summation convention over repeated indices. The displacement gradient with respect to the reference (initial) placement is called the deformation gradient:

$$F_{ij} = \frac{\partial u_i}{\partial X_j} + \delta_{ij}, \tag{3.3}$$

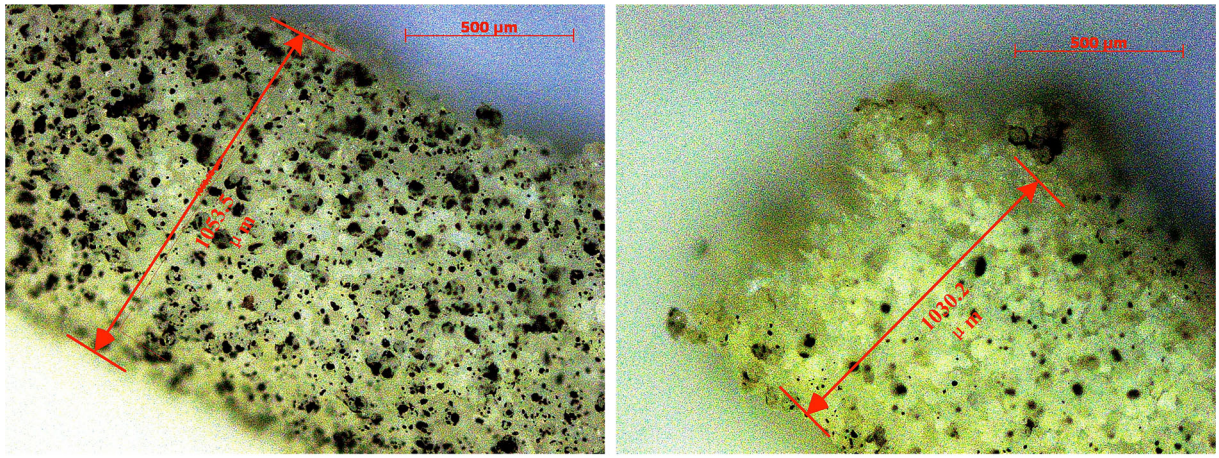

(a) (b)

FIG. 5. Microscope pictures of the sample used in the tensile test. **a** Beam before tensile test. **b** Beam after breaking

out of which we get the right Cauchy–Green deformation tensor, $\boldsymbol{C} = \boldsymbol{F}^\top \boldsymbol{F}$, as well as the left Cauchy–Green deformation tensor, $\boldsymbol{B} = \boldsymbol{F}\boldsymbol{F}^\top$. According to the Hamilton–Cayley theorem, a tensor in three-dimensional space possesses three invariants, I_1, I_2, I_3. Left and right deformation tensors have the same invariants. In a specially designed experiment, for example in a uni-, bi-, tri-axial tensile test, stretch ratio in one, two, three axes, $\lambda_i (i = 1, 2, 3)$ are used to connect the invariants to the measurable stretch as follows:

$$\begin{aligned} I_1 &= \mathrm{tr}(\boldsymbol{C}) = \mathrm{tr}(\boldsymbol{B}) = \lambda_1 + \lambda_2 + \lambda_3, \\ I_2 &= \frac{1}{2}\Big((\mathrm{tr}(\boldsymbol{C}))^2 - \mathrm{tr}(\boldsymbol{C}^2)\Big) = \frac{1}{2}\Big((\mathrm{tr}(\boldsymbol{B}))^2 - \mathrm{tr}(\boldsymbol{B}^2)\Big) = \lambda_1\lambda_2 + \lambda_2\lambda_3 + \lambda_3\lambda_1, \\ I_3 &= \det(\boldsymbol{C}) = \det(\boldsymbol{B}) = \lambda_1\lambda_2\lambda_3. \end{aligned} \tag{3.4}$$

The isochoric or incompressibility assumption leads to, $I_3 = 1$. In the case of a uniaxial tensile test shown in Fig. 3b, we realize

$$\lambda_1 \hat{=} \lambda \ , \quad \lambda_2 = \lambda_3 \hat{=} \frac{1}{\sqrt{\lambda}}, \tag{3.5}$$

effected by the incompressibility constraint. Hence, the deformation gradient and deformation tensor become

$$\boldsymbol{F} = \begin{pmatrix} \lambda & 0 & 0 \\ 0 & 1/\sqrt{\lambda} & 0 \\ 0 & 0 & 1/\sqrt{\lambda} \end{pmatrix} \ , \quad \boldsymbol{B} = \begin{pmatrix} \lambda^2 & 0 & 0 \\ 0 & 1/\lambda & 0 \\ 0 & 0 & 1/\lambda \end{pmatrix}. \tag{3.6}$$

The latter yields to the following invariants:

$$I_1 = \lambda^2 + \frac{2}{\lambda} \ , \quad I_2 = 2\lambda + \frac{1}{\lambda^2} \ , \quad I_3 = 1. \tag{3.7}$$

We search for a suitable stored energy density depending on the invariants, $W = W(I_1, I_2)$. The dependency is restricted by the so-called ellipticity, which is also called invertibility in the case of isotropic materials, in order to assure a smooth deformation gradient (continuity of $\boldsymbol{F}$), for details see [65]. The ellipticity holds in every single argument, which is often called quasiconvexity. The choice of the functional form and the material constants shall not violate the quasiconvexity for obtaining sufficient smoothness in the deformation gradient. There are several hyperelastic models satisfying quasiconvexity in the literature. They can be sorted into three groups. The first group covers Mooney–Rivlin, Biderman, Haine–Wilson,

and Yeoh models. They are all motivated by using representation theorems and constructed phenomenologically. Second group includes Rivlin–Saunders, Hart–Smith, and Gent models; the material functions of these models are determined as the best fitting curve to the experimental data. To the third group, we can name neo-Hooke, Isihara, Arruda–Boyce models justified by statistical average of microscopic models at the length scale of polymer chains.

We present the results for St. Venant–Kirchhoff model (will be denoted by SV), Mooney–Rivlin models with 2 and 5 parameters (MR2, MR5), Biderman model (Bi), Haine–Wilson model (HW), neo-Hookean model (Neo), Isihara model (Is), and Yeoh model (Yeoh). St. Venant–Kirchhoff model reads

$$W = \frac{\lambda}{2}\big(\operatorname{tr}(\boldsymbol{E})\big)^2 + \mu \operatorname{tr}(\boldsymbol{E}^2)\ , \quad \boldsymbol{E} = \frac{1}{2}(\boldsymbol{C} - \boldsymbol{\delta}), \tag{3.8}$$

where we use the Green–Lagrange strain tensor, $\boldsymbol{E}$, and two so-called Lame parameters, λ and μ. This model has been utilized to analyze the deformation of the pantographic structure in [34]. Mooney–Rivlin model as in [54,64] shows good accuracy in predicting the nonlinear behavior of rubber-like materials. The general form of the energy density function according to Mooney–Rivlin model reads

$$W = \sum_{i=0,j=0}^{\infty} C_{ij}(I_1 - 3)^i (I_2 - 3)^j, \tag{3.9}$$

where C_{ij} are material parameters to be determined by experiments, obviously, $C_{00} = 0$. Truncating the series gives the widely used forms of Mooney–Rivlin models with 2 and 5 parameters,

$$\begin{aligned} W_{\mathrm{MR2}} &= C_{10}(I_1 - 3) + C_{01}(I_2 - 3), \\ W_{\mathrm{MR5}} &= C_{10}(I_1 - 3) + C_{01}(I_2 - 3) + C_{11}(I_1 - 3)(I_2 - 3) + C_{20}(I_1 - 3)^2 + C_{02}(I_2 - 3)^2. \end{aligned} \tag{3.10}$$

The well-known neo-Hookean model,

$$W = C_{10}(I_1 - 3), \tag{3.11}$$

is motivated by a network of randomly oriented molecular chains, see [32,46,72]. Truncating the Mooney–Rivlin series to one order and set $C_{01} = 0$ will also lead to the neo-Hookean model, although the justifications of both models differ. Preserving Mooney–Rivlin series with $i = 0$ or $j = 0$ and taking first three terms for I_1 and one term for I_2 generates Biderman's model [16] in the following form:

$$W_{\mathrm{Bi}} = C_{10}(I_1 - 3) + C_{01}(I_2 - 3) + C_{20}(I_1 - 3)^2 + C_{30}(I_1 - 3)^3. \tag{3.12}$$

Moreover, the Haines–Wilson model proposed in [41] contains six terms, in which I_1 and I_2 are extended to third and second order, respectively,

$$W_{\mathrm{HW}} = C_{10}(I_1 - 3) + C_{01}(I_2 - 3) + C_{11}(I_1 - 3)(I_2 - 3) + C_{20}(I_1 - 3)^2 + C_{02}(I_2 - 3)^2 + C_{30}(I_1 - 3)^3 \tag{3.13}$$

Isiharain model as in [39] is another statistical model by using non-Gaussian distribution of polymer chains network. Isiharain model reads

$$W_{Is} = C_{10}(I_1 - 3) + C_{01}(I_2 - 3) + C_{20}(I_1 - 3)^2, \tag{3.14}$$

resembling the Mooney–Rivlin series as well. As proposed in [77], Yeoh model is based on the first invariant. We use the Yeoh model with three terms,

$$W_{\mathrm{Yeoh}} = C_{10}(I_1 - 3) + C_{20}(I_1 - 3)^2 + C_{30}(I_1 - 3)^3. \tag{3.15}$$

We examine all models by using an inverse analysis and compare their capabilities related to how accurately each of them fits the experimental data.

3.3. Inverse analysis

The constitutive equation is given by the stored energy as a scalar nonlinear function depending on invariants of the deformation tensor. Because of the nonlinearity, a nonlinear regression as Levenberg–Marquardt method is frequently used to fit the parameters, see [42,47]. Success of a nonlinear regression depends on a good initial estimation of the parameters. Especially in hyperelastic material models, initial estimation can be very challenging. As a possible remedy, we present herein the energy-based method proposed in [1, Sect. 9] and applied in [4] for another type of experiments. By using the energy-based method, we generate a linear regression problem for determining the material parameters uniquely. In other words, there is only one solution of the best material parameters minimizing the square of the error between measurement and estimation. This method is possible since all models are linear in the material parameters. In the case of the Mooney–Rivlin model with 2 parameters, we use the energy value at n points by exploiting the numerical integration in Eq. (3.2) out of the experimental data and compute the energy with the unknown material parameters,

$$\begin{pmatrix} \left(\lambda_1^2+\frac{2}{\lambda_1}-3\right) & \left(2\lambda_1+\frac{1}{\lambda_1^2}-3\right) \\ \left(\lambda_2^2+\frac{2}{\lambda_2}-3\right) & \left(2\lambda_2+\frac{1}{\lambda_2^2}-3\right) \\ \vdots & \vdots \\ \left(\lambda_n^2+\frac{2}{\lambda_n}-3\right) & \left(2\lambda_n+\frac{1}{\lambda_n^2}-3\right) \end{pmatrix} \begin{pmatrix} C_{10} \\ C_{01} \end{pmatrix} = \begin{pmatrix} W_1^{\mathrm{MR2}} \\ W_2^{\mathrm{MR2}} \\ \vdots \\ W_n^{\mathrm{MR2}} \end{pmatrix}. \tag{3.16}$$

The latter can be written as

$$A_{ij}c_j = b_i \ , \quad i=\{1,2,3,\ldots,n\} \ , \quad j=\{1,2,3,\ldots m\} \tag{3.17}$$

such that the right-hand side is known from the experiments, $\boldsymbol{A}$ can be computed as well, and $\boldsymbol{c}$ denotes m unknown coefficients—the material parameters to be determined. The number of experimental data, n, is more than the unknowns, m, hence, we cannot solve the system exactly. An approximation to this problem is found by setting the goal as minimizing the error (square) between the estimation and the experimental data. We search for the best set of unknowns $\hat{\boldsymbol{c}}$ in the sense of least squared error and obtain the so-called normal equation,

$$\hat{\boldsymbol{c}} = \boldsymbol{A}^{+}\boldsymbol{b} = (\boldsymbol{A}^{\top}\boldsymbol{A})^{-1}\boldsymbol{A}^{\top}\boldsymbol{b}, \tag{3.18}$$

where $\boldsymbol{A}^{+}$ is the pseudoinverse of the matrix $\boldsymbol{A}$. The Eq. (3.18) is well known in statistics; we refer to [4] for its derivation. We emphasize that the linear regression leads to the unique set of coefficients. Even in the case of a nonlinear material model, the presented approach yields to a linear regression problem. Solving such a system is simple and fast.

We have compiled in Fig. 6 the results of the linear regression, in which black solid line represents experimental data and red dashed line denotes the fit curve. We use R-squared (R^2) as an indicator of the accuracy of the fit curve. It is a statistical measure defined as follows:

$$R^2 = 1 - \frac{S_{\mathrm{res}}}{S_{\mathrm{tot}}}, \tag{3.19}$$

using the total sum of squares, S_{tot}, and the residual sum of squares, S_{res}, i.e.,

$$S_{\mathrm{tot}} = \sum_i (y_i - \bar{y})^2 \ , \quad S_{\mathrm{res}} = \sum_i (y_i - f_i)^2, \tag{3.20}$$

where f_i symbolizes the fitted data, for a data set with n values marked by $y_1 \ldots y_i \ldots y_n$ and the mean value is

$$\bar{y} = \frac{1}{n}\sum_{i=1}^{n} y_i. \tag{3.21}$$

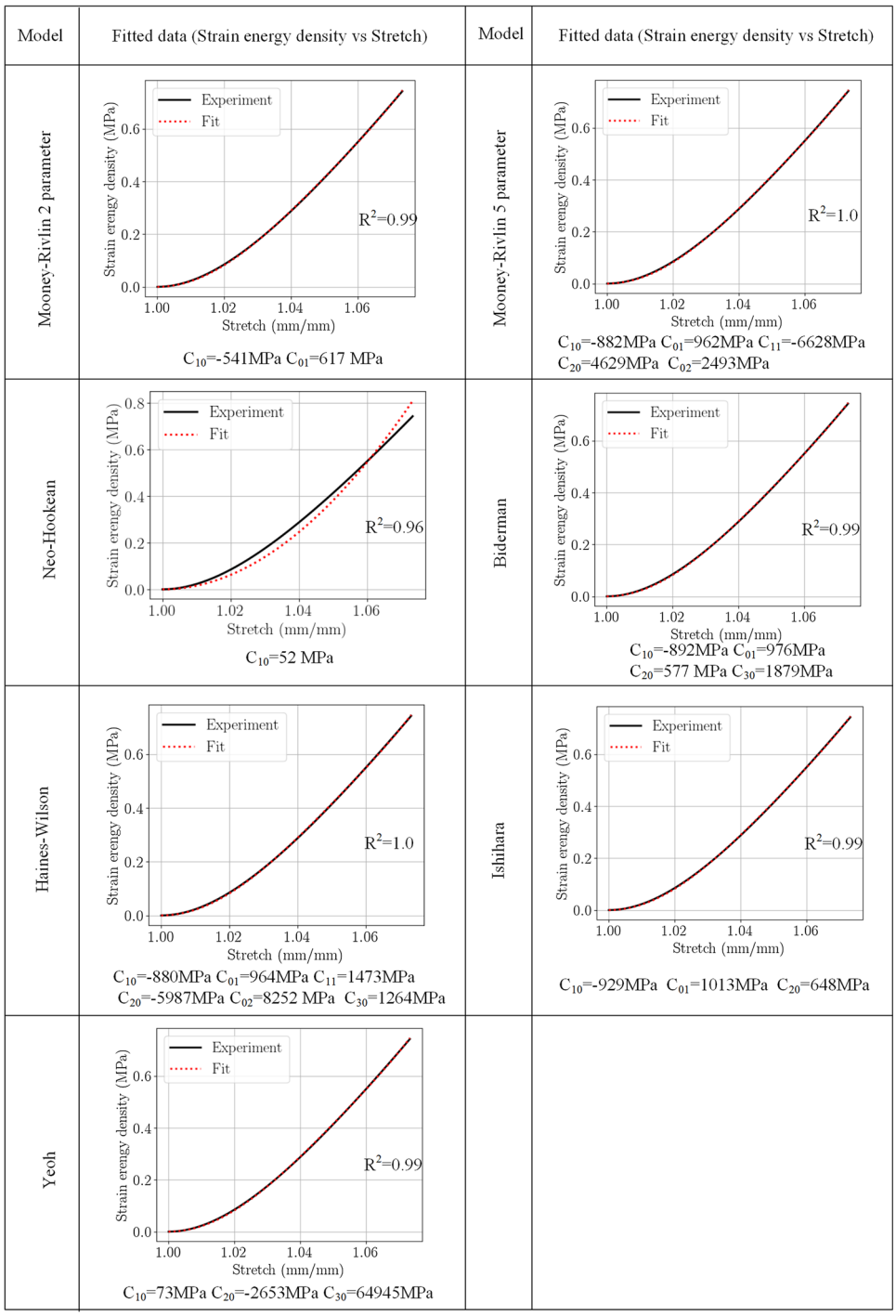

FIG. 6. Data fitting of different material models. Black continuous line is the experimental data and red dashed line shows the corresponding fit curve. On the horizontal axis stretch, λ, and on the vertical axis the strain (or stored) energy density, W, are written. C_{ij} are the material parameters in different models

Table 2. *Comparison of hyperelastic models*

Model	Year	Number of parameters	Variables	Type	R^2
MR2	1940	2	I_1, I_2	Phenomenological	0.99
MR5	1948	5	$I_1, I_2, I_1^2, I_2^2, I_1 I_2$	Phenomenological	1.0
Neo	1943	1	I_1	Mechanistic	0.96
Bi	1958	4	I_1, I_2, I_1^2, I_1^3	Phenomenological	0.99
HW	1975	6	$I_1, I_2, I_1 I_2, I_1^2, I_2^2, I_1^3$	Phenomenological	1.0
Is	1951	3	I_1, I_2, I_1^2	Mechanistic	0.99
Yeoh	1993	3	I_1, I_1^2, I_1^3	Phenomenological	0.99

By using the normal equation (3.18), we have obtained the fit curves. A comparison of all applied hyperelastic models with their corresponding R^2 values are summarized in Table 2.

All models have a fairly good agreement to the experimental data. Mooney–Rivlin model with 5 parameters and Haines–Wilson model have both a R^2 of 1.0, indicating that the constitutive equation perfectly model materials response. In contrast, neo-Hookean model shows a relatively poorer fit with a R^2 of 0.96. We emphasize that we use a uniaxial tensile test and want to generalize the outcome for any other type of deformation. From the inverse analysis in this section, one may think that any model might be used to simulate the experiment in Sect. 2. We will show, unfortunately, that this fact fails to be true.

4. Direct numerical simulation

We essentially follow [3] and start with the Lagrange an possessing kinetic energy, stored energy, and potential energy because of gravity. We assume that the deformation because of inertial effects as well as the weight are negligible. After a variational formulation, we obtain the weak form:

$$\Pi = \int_{\Omega} \frac{\partial W}{\partial u_{i,j}} \delta u_{i,j} \, \mathrm{d}V - \int_{\partial\Omega} \hat{t}_i \delta u_i \, \mathrm{d}A, \tag{4.1}$$

for a domain $\Omega \subset \mathbb{R}^3$ occupied by the continuum body, under Dirichlet boundary conditions, where the displacement is given, or under Neumann boundary conditions, where the traction vector $\hat{t}_i$ is prescribed. The latter integral form vanishes, $\Pi = 0$, in the case of correct displacements, $\boldsymbol{u} = 0$, but it is nonlinear in displacements such that we need to linearize it by using the Newton–Raphson formalism. The solution is found in an incremental manner,

$$\boldsymbol{u} := \boldsymbol{u} + \Delta\boldsymbol{u}, \tag{4.2}$$

where the numerical value of $\boldsymbol{u}$ is overwritten in each increment by $\boldsymbol{u} + \Delta\boldsymbol{u}$. By using standard argumentation for linearization, we obtain

$$\Pi + \boldsymbol{J} \cdot \Delta\boldsymbol{u} = 0, \tag{4.3}$$

with the Jacobian $\boldsymbol{J} = \partial\Pi/\partial\boldsymbol{u}$ and the Gateaux derivative:

$$\boldsymbol{J} \cdot \Delta\boldsymbol{u} = \lim_{\varepsilon \to 0} \frac{\mathrm{d}}{\mathrm{d}\varepsilon} \Pi(\boldsymbol{u} + \varepsilon \Delta\boldsymbol{u}). \tag{4.4}$$

For the computation we exploit open-source packages developed under the FEniCS project [37]. Python language is used for implementing the geometry, boundary conditions, weak form, and its Jacobian. Especially for the linearization, the Newton–Raphson formalism is employed by using a symbolic derivative at the level of partial differential equations such that all hyperelastic material models are applied just by renewing their definition. The CAD models of the pantographic samples were built by the open-source platform SALOME 7. The triangulation, i.e., FEM discretization in space has been established with the aid of the mesh generator NetGen, already built-in SALOME 7. These steps are presented in detail in [2, Appendix 3]. Paraview 5 is used to post-process the results.

Quadratic tetrahedron elements are used in order to achieve a high element quality in meshing the complicated geometry. As a consequence of a standard h-convergence analysis—decreasing size of each element in the domain results in a solution with higher accuracy—we have determined a model with approximately 3 million degrees of freedom. The computations are established on 16 CPUs (Intel Xeon E7-4850 on SuperMicro server) by using mpirun for about 4 h. As in the experiments, one side of the whole structure is clamped by setting displacements in all directions zero. On the other side, prescribed displacement from up to 70 mm has been employed in 1 mm increments. The geometric nonlinearities necessitate to linearize and solve by using an initial estimation. Although the simulation is for the quasi-static case, the solution from the previous step is used as the initial estimation in linearization. This approach is sometimes called the arc-length method. From the experiments, we know an out-of-plane displacement in shear test. We intend to investigate this specific deformation pattern. For circumventing any bifurcation, as suggested in [35], we apply additional forces of 1 mN at the positions where the out-of-plane displacement is expected. In the experiments, the total reaction force is measured. In the corresponding simulations, reaction force along the shear direction is computed by summing the nodal forces on this boundary.

5. Comparison of computations with experiments

We perform the experiments undertaken in Sect. 2 as seen in Fig. 2. A possible comparison can be done using the measured reaction force as the prescribed displacement is applied. Several hyperelastic models are employed and all computational results are summarized in Fig. 7. Yeoh model (Yeoh) shows an outstanding match with respect to other models—especially for displacements greater than 20 mm. We remark that all used hyperelastic models are evaluated by using the parameters as determined and shown in Fig. 6. Hence, it is challenging to justify, why a particular model performs significantly better. As expected, the linear St. Venant–Kirchhoff model (SV) starts deviating from the experimental results for displacements greater than 15 mm. Biderman model (Bi), Haine–Wilson model (HW), and Isihara model (Is) generate the same result with an adequate matching to the experiment up to 20 mm of the prescribed displacement. They are identical to Mooney–Rivlin model with 5 parameters (MR5) up to 45 mm prescribed displacements. A possible explanation to the distinction among the models is as follows: Yeoh model possesses only the first invariant of the deformation tensor, but the other models incorporate the second invariant as well. By using the uniaxial tensile testing, we fail to identify accurately the material parameters responsible for a shearing deformation mainly given by the second invariant. Therefore, we conclude hypothetically that a combination of tests would result in Bi-HW-Is-MR5 hyperelastic material models' parameters matching the experiments as good as Yeoh model.

Furthermore, we investigate the out-of-plane behavior by comparing the computation of Yeoh model with the experimental result in Fig. 8 when the maximum displacement of 70 mm has been reached. The experimental result is post-processed by using a digital image correlation (DIC), see [12] for details. Upper left part displacement is missing as a consequence of setting the focus of the camera to the out-of-plane displacement. Qualitatively, the experimental and numerical results are identical: the maximum values of displacement are both located at the lower left corner. Quantitatively, their results have 2.3% deviation: simulation calculates the maximum displacement of 20.5 mm, whereas the experiment measures 19.6 mm. Additionally, we present in Fig. 9 the out-of-plane displacement at the point of maximum deflection over the whole simulation and experiment. All constitutive models describe this behavior fairly well. St. Venant–Kirchhoff model (SV), Biderman model (Bi), Isihara model (Is), and Haine–Wilson model (HW) show the same behavior. Analogously, Mooney–Rivlin with 5 parameters (MR5) and Yeoh model have the same out-of-plane movements. Qualitatively, numerical results are adequate. We emphasize that experiments involve errors as well. We know that the initial out-of-plane deflection in experiments is sensitive to the accuracy in the colinearity between the adaption device. The deviations between the

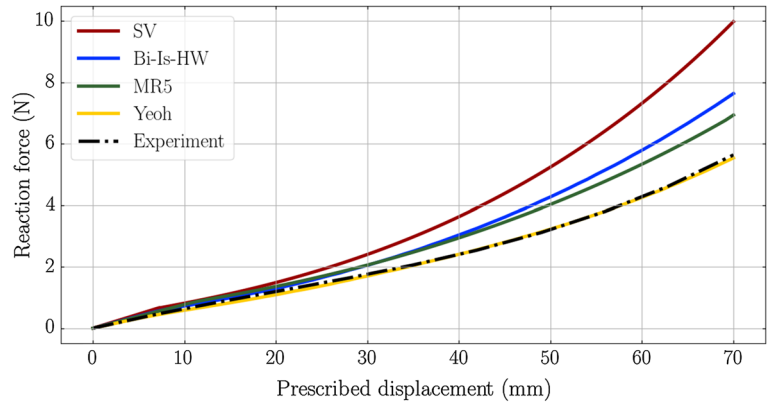

FIG. 7. Reaction force in the displacement controlled shear test: experiment (dash-dotted line); numerical simulations (solid lines)

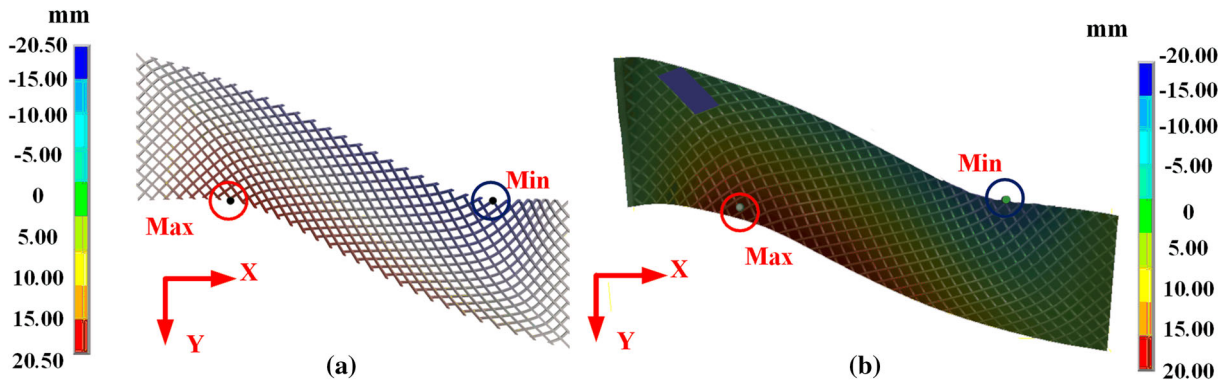

FIG. 8. Deformation obtained from the computation by using Yeoh model (left) and experimental results acquired by a digital image correlation (right)

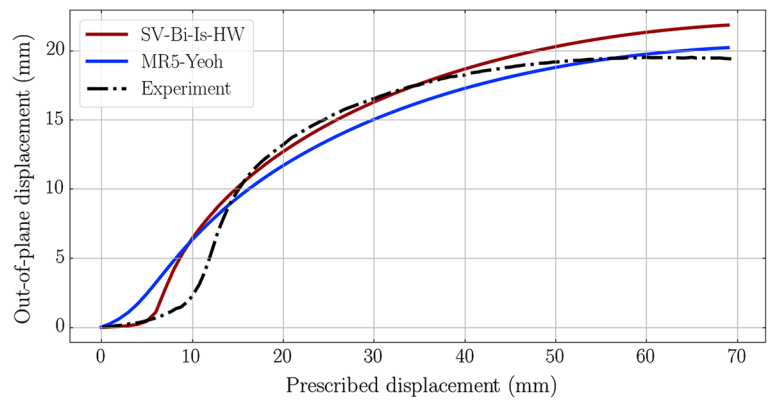

FIG. 9. Out-of-plane displacement versus applied shearing displacement

experimental and computational results are justified by the fact that the boundary conditions in the experiments lack the high accuracy necessary to detect this behavior quantitatively.

We encourage to investigate this phenomenon by using two-dimensional continuum models as they describe similar effects with a fraction of the computational cost used herein. Such models, for example as in [35,66], can be compared with the experimental results and shed more light on the complex deformation pattern because of the substructure by means of a micro-macro identification.

6. Conclusions

Metamaterials possess an internal substructure leading to unconventional deformation patterns. In this work, we have analyzed a 3D printed pantographic structure made of laser-sintered polyamide (PA). Shearing experiments are conducted, and their computational modeling has been rigorously discussed by using simulations realized with the help of open-source codes in the FEniCS platform. For a successful material modeling, additional uniaxial tensile tests are undertaken leading to a necessity of a nonlinear material behavior. We have discussed various hyperelastic material models and used a novel method for determining the material parameters. The comparison between the numerical and experimental results is carried out by using reaction force and displacement. We emphasize that the whole study is necessary to gain a better understanding of systems with an internal substructure. The pantographic structure is only a very simple example to study the effect of a substructure at macroscopic length scale. Indeed, the study of the response at microscopic length scale can lead to a possible explanation of unconventional materials response.

Acknowledgements

IG is supported by a grant from the Government of the Russian Federation (No. 14.Y26.31.0031). We thank Prof. Wolfgang H. Müller for fruitful discussions.

References

[1] Abali, B.E.: Thermodynamically Compatible Modeling, Determination of Material Parameters, and Numerical Analysis of Nonlinear Rheological Materials. PhD thesis, Technische Universität Berlin, Institute of Mechanics (2014)
[2] Abali, B.E.: Computational Reality, Solving Nonlinear and Coupled Problems in Continuum Mechanics. Advanced Structured Materials. Springer, Berlin (2017)
[3] Abali, B.E., Müller, W.H., dell'Isola, F.: Theory and computation of higher gradient elasticity theories based on action principles. Arch. Appl. Mech. **87**(9), 1495–1510 (2017)
[4] Abali, B.E., Wu, C.-C., Müller, W.H.: An energy-based method to determine material constants in nonlinear rheology with applications. Contin. Mech. Thermodyn. **28**(5), 1221–1246 (2016)
[5] Alibert, J.-J., Seppecher, P., dell'Isola, F.: Truss modular beams with deformation energy depending on higher displacement gradients. Math. Mech. Solids **8**(1), 51–73 (2003)
[6] Altenbach, H., Eremeyev, V.A.: Analysis of the viscoelastic behavior of plates made of functionally graded materials. ZAMM-Zeitschrift für Angewandte Mathematik und Mechanik **88**(5), 332–341 (2008)
[7] Altenbach, H., Eremeyev, V.A. (eds.): Generalized Continua—from the Theory to Engineering Applications, Volume 541 of CISM International Centre for Mechanical Sciences. Springer, Wien (2013)
[8] Altenbach, H., Eremeyev, V.A.: Surface viscoelasticity and effective properties of materials and structures. In: Altenbach, H., Kruch, S. (eds.) Advanced Materials Modelling for Structures, pp. 9–16. Springer, Berlin (2013)
[9] Andreaus, U., Spagnuolo, M., Lekszycki, T., Eugster, S.R.: A Ritz approach for the static analysis of planar pantographic structures modeled with nonlinear Euler–Bernoulli beams. Contin. Mech. Thermodyn. (2018). https://doi.org/10.1007/s00161-018-0665-3
[10] Arruda, E.M., Boyce, M.C.: A three-dimensional constitutive model for the large stretch behavior of rubber elastic materials. J. Mech. Phys. Solids **41**(2), 389–412 (1993)

[11] Attard, M.M., Hunt, G.W.: Hyperelastic constitutive modeling under finite strain. Int. J. Solids Struct. **41**(18–19), 5327–5350 (2004)
[12] Barchiesi, E., Ganzosch, G., Liebold, C., Placidi, L., Grygoruk, R., Müller, W.H.: Out-of-plane buckling of pantographic fabrics in displacement-controlled shear tests: experimental results and model validation. Contin. Mech. Thermodyn. (2018). https://doi.org/10.1007/s00161-018-0626-x
[13] Barchiesi, E., Spagnuolo, M., Placidi, L.: Mechanical metamaterials: a state of the art. Math. Mech. Solids (2018). https://doi.org/10.1177/1081286517735695
[14] Battista, A., Cardillo, C., Del Vescovo, D., Rizzi, N.L., Turco, E.: Frequency shifts induced by large deformations in planar pantographic continua. Nanosci. Technol. Int. J. **6**(2), 161–178 (2015)
[15] Battista, A., Del Vescovo, D., Rizzi, N.L., Turco, E.: Frequency shifts in natural vibrations in pantographic metamaterials under biaxial tests. Technische Mechanik **37**(1), 1–17 (2017)
[16] Biderman, V.L.: Calculation of rubber parts. Rascheti na prochnost, Moscow (1958)
[17] Boutin, C., dell'Isola, F., Giorgio, I., Placidi, L.: Linear pantographic sheets: asymptotic micro-macro models identification. Math. Mech. Complex Syst. **5**(2), 127–162 (2017)
[18] Cuomo, M.: Forms of the dissipation function for a class of viscoplastic models. Math. Mech. Complex Syst. **5**(3), 217–237 (2017)
[19] De Masi, A., Merola, I., Presutti, E., Vignaud, Y.: Coexistence of ordered and disordered phases in Potts models in the continuum. J. Stat. Phys. **134**(2), 243–306 (2009)
[20] Del Vescovo, D., Giorgio, I.: Dynamic problems for metamaterials: review of existing models and ideas for further research. Int. J. Eng. Sci. **80**, 153–172 (2014)
[21] dell'Isola, F., Andreaus, U., Placidi, L.: At the origins and in the vanguard of peridynamics, non-local and higher-gradient continuum mechanics: an underestimated and still topical contribution of gabrio piola. Math. Mech. Solids **20**, 887–928 (2014)
[22] dell'Isola, F., Della Corte, A., Giorgio, I.: Higher-gradient continua: the legacy of Piola, Mindlin, Sedov and Toupin and some future research perspectives. Math. Mech. Solids **22**(4), 852–872 (2017)
[23] dell'Isola, F., Giorgio, I., Pawlikowski, M., Rizzi, N.L.: Large deformations of planar extensible beams and pantographic lattices: heuristic homogenization, experimental and numerical examples of equilibrium. Proc. R. Soc. A **472**(2185), 1–23 (2016)
[24] dell'Isola, F., Lekszycki, T., Pawlikowski, M., Grygoruk, R., Greco, L.: Designing a light fabric metamaterial being highly macroscopically tough under directional extension: first experimental evidence. Zeitschrift für angewandte Mathematik und Physik **66**(6), 3473–3498 (2015)
[25] dell'Isola, F., Seppecher, P., et al.: Pantographic metamaterials: an example of mathematically driven design and of its technological challenges. Contin. Mech. Thermodyn. (2018). https://doi.org/10.1007/s00161-018-0689-8
[26] dell'Isola, F., Steigmann, D., Della Corte, A.: Synthesis of fibrous complex structures: designing microstructure to deliver targeted macroscale response. Appl. Mech. Rev. **67**(6), 060804 (2015)
[27] Diyaroglu, C., Oterkus, E., Oterkus, S., Madenci, E.: Peridynamics for bending of beams and plates with transverse shear deformation. Int. J. Solids Struct. **69**, 152–168 (2015)
[28] Engelbrecht, J., Berezovski, A.: Reflections on mathematical models of deformation waves in elastic microstructured solids. Math. Mech. Complex Syst. **3**(1), 43–82 (2015)
[29] Eremeyev, V.A., Pietraszkiewicz, W.: Material symmetry group and constitutive equations of micropolar anisotropic elastic solids. Math. Mech. Solids **21**(2), 210–221 (2016)
[30] Eringen, A.C.: Theory of Micropolar Elasticity. Technical report, DTIC Document (1967)
[31] Eugster, S.R., Hesch, C., Betsch, P., Glocker, C.: Director-based beam finite elements relying on the geometrically exact beam theory formulated in skew coordinates. Int. J. Numer. Methods Eng. **97**(2), 111–129 (2014)
[32] Flory, P.J., Rehner Jr., J.: Statistical mechanics of cross-linked polymer networks I. Rubberlike elasticity. J. Chem. Phys. **11**(11), 512–520 (1943)
[33] Ganzosch, G., dell'Isola, F., Turco, E., Lekszycki, T., Müller, W.H.: Shearing tests applied to pantographic structures. Acta Polytech. CTU Proc. **7**, 1–6 (2016)
[34] Giorgio, I.: Numerical identification procedure between a micro-Cauchy model and a macro-second gradient model for planar pantographic structures. Zeitschrift für angewandte Mathematik und Physik **67**(4), 95 (2016)
[35] Giorgio, I., Rizzi, N.L., Turco, E.: Continuum modelling of pantographic sheets for out-of-plane bifurcation and vibrational analysis. Proc. R. Soc. A **473**(2207), 1–21 (2017)
[36] Harrison, P., Clifford, M.J., Long, A.C., Rudd, C.D.: A constituent-based predictive approach to modelling the rheology of viscous textile composites. Compos. A Appl. Sci. Manuf. **35**(7–8), 915–931 (2004)
[37] Hoffman, J., Jansson, J., Johnson, C., Knepley, M., Kirby, R.C., Logg, A., Scott, L.R., Wells, G.N.: Fenics (2005). http://www.fenicsproject.org/
[38] Holzapfel, A.G.: Nonlinear Solid Mechanics II. Wiley, New York (2000)
[39] Isihara, A., Hashitsume, N., Tatibana, M.: Statistical theory of rubber-like elasticity. IV (two-dimensional stretching). J. Chem. Phys. **19**(12), 1508–1512 (1951)

[40] Itskov, M., Aksel, N.: A class of orthotropic and transversely isotropic hyperelastic constitutive models based on a polyconvex strain energy function. Int. J. Solids Struct. **41**(14), 3833–3848 (2004)
[41] James, A.G., Green, A., Simpson, G.M.: Strain energy functions of rubber. I. Characterization of gum vulcanizates. J. Appl. Polym. Sci. **19**(7), 2033–2058 (1975)
[42] Julio García Ruíz, M., Yarime Suárez González, L.: Comparison of hyperelastic material models in the analysis of fabrics. Int. J. Cloth. Sci. Technol. **18**(5), 314–325 (2006)
[43] Khakalo, S., Balobanov, V., Niiranen, J.: Modelling size-dependent bending, buckling and vibrations of 2D triangular lattices by strain gradient elasticity models: applications to sandwich beams and auxetics. Int. J. Eng. Sci. **127**, 33–52 (2018)
[44] Lam, D.C.C., Yang, F., Chong, A.C.M., Wang, J., Tong, P.: Experiments and theory in strain gradient elasticity. J. Mech. Phys. Solids **51**(8), 1477–1508 (2003)
[45] Logg, A., Mardal, K.A., Wells, G.N.: Automated Solution of Differential Equations by the Finite Element Method, the FEniCS Book, Volume 84 of Lecture Notes in Computational Science and Engineering. Springer, Berlin (2011)
[46] Marckmann, G., Verron, E.: Comparison of hyperelastic models for rubber-like materials. Rubber Chem. Technol. **79**(5), 835–858 (2006)
[47] Martins, P., Natal Jorge, R.M., Ferreira, A.J.M.: A comparative study of several material models for prediction of hyperelastic properties: application to silicone-rubber and soft tissues. Strain **42**(3), 135–147 (2006)
[48] Milton, G.W., Briane, M., Harutyunyan, D.: On the possible effective elasticity tensors of 2-dimensional and 3-dimensional printed materials. Math. Mech. Complex Syst. **5**(1), 41–94 (2017)
[49] Mindlin, R.D., Eshel, N.N.: On first strain–gradient theories in linear elasticity. Int. J. Solids Struct. **4**(1), 109–124 (1968)
[50] Mindlin, R.D., Tiersten, H.F.: Effects of couple-stresses in linear elasticity. Arch. Ration. Mech. Anal. **11**, 415–448 (1962)
[51] Misra, A., Lekszycki, T., Giorgio, I., Ganzosch, G., Müller, W.H., dell'Isola, F.: Pantographic metamaterials show atypical Poynting effect reversal. Mech. Res. Commun. **89**, 6–10 (2018)
[52] Misra, A., Poorsolhjouy, P.: Identification of higher-order elastic constants for grain assemblies based upon granular micromechanics. Math. Mech. Complex Syst. **3**(3), 285–308 (2015)
[53] Misra, A., Poorsolhjouy, P.: Granular micromechanics based micromorphic model predicts frequency band gaps. Contin. Mech. Thermodyn. **28**(1–2), 215–234 (2016)
[54] Mooney, M.: A theory of large elastic deformation. J. Appl. Phys. **11**(9), 582–592 (1940)
[55] Nadler, B., Papadopoulos, P., Steigmann, D.J.: Multiscale constitutive modeling and numerical simulation of fabric material. Int. J. Solids Struct. **43**(2), 206–221 (2006)
[56] Niiranen, J., Balobanov, V., Kiendl, J., Hosseini, S.B.: Variational formulations, model comparisons and numerical methods for Euler–Bernoulli micro-and nano-beam models. Math. Mech. Solids (2017). https://doi.org/10.1177/1081286517739669
[57] Pideri, C., Seppecher, P.: A second gradient material resulting from the homogenization of an heterogeneous linear elastic medium. Contin. Mech. Thermodyn. **9**(5), 241–257 (1997)
[58] Placidi, L., Andreaus, U., Della Corte, A., Lekszycki, T.: Gedanken experiments for the determination of two-dimensional linear second gradient elasticity coefficients. Zeitschrift für angewandte Mathematik und Physik **66**(6), 3699–3725 (2015)
[59] Placidi, L., Barchiesi, E.: Energy approach to brittle fracture in strain-gradient modelling. Proc. R. Soc. A **474**(2210), 1–19 (2018)
[60] Placidi, L., Barchiesi, E., Battista, A.: An inverse method to get further analytical solutions for a class of metamaterials aimed to validate numerical integrations. In: dell'Isola, F., Sofonea, M., Steigmann, D. (eds.) Mathematical Modelling in Solid Mechanics, pp. 193–210. Springer, Berlin(2017)
[61] Placidi, L., Barchiesi, E., Misra, A.: A strain gradient variational approach to damage: a comparison with damage gradient models and numerical results. Math. Mech. Complex Syst. **6**(2), 77–100 (2018)
[62] Placidi, L., Barchiesi, E., Turco, E., Rizzi, N.L.: A review on 2D models for the description of pantographic fabrics. Zeitschrift für angewandte Mathematik und Physik **67**(5), 121 (2016)
[63] Placidi, L., Misra, A., Barchiesi, E.: Two-dimensional strain gradient damage modeling: a variational approach. Zeitschrift für angewandte Mathematik und Physik **69**(3), 1–19 (2018)
[64] Rivlin, R.S.: Large elastic deformations of isotropic materials iv. further developments of the general theory. Philos. Trans. R. Soc. Lond. A **241**(835), 379–397 (1948)
[65] Rosakis, P.: Ellipticity and deformations with discontinuous gradients in finite elastostatics. Arch. Ration. Mech. Anal. **109**(1), 1–37 (1990)
[66] Shirani, M., Luo, C., Steigmann, D.J.: Cosserat elasticity of lattice shells with kinematically independent flexure and twist. Contin. Mech. Thermodyn. (2018). https://doi.org/10.1007/s00161-018-0679-x
[67] Soe, S.P., Martindale, N., Constantinou, C., Robinson, M.: Mechanical characterisation of Duraform® Flex for FEA hyperelastic material modelling. Polym. Test. **34**, 103–112 (2014)

[68] Spagnuolo, M., Barcz, K., Pfaff, A., dell'Isola, F., Franciosi, P.: Qualitative pivot damage analysis in aluminum printed pantographic sheets: numerics and experiments. Mech. Res. Commun. **83**, 47–52 (2017)
[69] Steigmann, D.J., dell'Isola, F.: Mechanical response of fabric sheets to three-dimensional bending, twisting, and stretching. Acta. Mech. Sin. **31**(3), 373–382 (2015)
[70] Thai, H.-T., Vo, T.P., Nguyen, T.-K., Kim, S.-E.: A review of continuum mechanics models for size-dependent analysis of beams and plates. Compos. Struct. **177**, 196–219 (2017)
[71] Toupin, R.A.: Theories of elasticity with couple-stress. Arch. Ration. Mech. Anal. **17**(2), 85–112 (1964)
[72] Treloar, L.R.G.: The elasticity of a network of long-chain molecules—II. Trans. Faraday Soc. **39**, 241–246 (1943)
[73] Turco, E., dell'Isola, F., Cazzani, A., Rizzi, N.L.: Hencky-type discrete model for pantographic structures: numerical comparison with second gradient continuum models. Zeitschrift für angewandte Mathematik und Physik **67**(4), 85 (2016)
[74] Turco, E., dell'Isola, F., Rizzi, N.L., Grygoruk, R., Müller, W.H., Liebold, C.: Fiber rupture in sheared planar pantographic sheets: numerical and experimental evidence. Mech. Res. Commun. **76**, 86–90 (2016)
[75] Turco, E., Giorgio, I., Misra, A., dell'Isola, F.: King post truss as a motif for internal structure of (meta) material with controlled elastic properties. R. Soc. Open Sci. **4**(10), 171153 (2017)
[76] Weber, G., Anand, L.: Finite deformation constitutive equations and a time integration procedure for isotropic, hyperelastic–viscoplastic solids. Comput. Methods Appl. Mech. Eng. **79**(2), 173–202 (1990)
[77] Yeoh, O.H.: Some forms of the strain energy function for rubber. Rubber Chem. Technol. **66**(5), 754–771 (1993)

Hua Yang, Gregor Ganzosch and B. Emek Abali
Chair of Continuum Mechanics and Constitutive Theory, Institute of Mechanics
Technische Universität Berlin
Einsteinufer 5
10587 Berlin
Germany
e-mail: hua.yang@campus.tu-berlin.de

Gregor Ganzosch
e-mail: ganzosch@tu-berlin.de

B. Emek Abali
e-mail: bilenemek@abali.org

Ivan Giorgio
International Research Center for the Mathematics and Mechanics of Complex Systems
Università degli studi dell'Aquila
L'Aquila
Italy

Ivan Giorgio
Department of Mechanical and Aerospace Engineering
Sapienza Università di Roma
Via Eudossiana 18
00184 Rome
Italy
e-mail: ivan.giorgio@uniroma1.it

Ivan Giorgio
Research Institute for Mechanics, National Research Lobachevsky
State University of Nizhni Novgorod
Nizhni Novgorod
Russian Federation

(Received: May 9, 2018; revised: July 14, 2018)